SUPPLEMENTAL INFORMATION

Random Field Reconstruction of Three-Phase Polymer Structures with Anisotropy from 2D-Small-Angle Scattering Data

Stephen Kronenberger[1], Nitant Gupta[1], Benjamin Gould[2], Colin Peterson[2], Arthi Jayaraman*[1,3,4]

1. Department of Chemical and Biomolecular Engineering, University of Delaware, Colburn Lab, 150 Academy Street, Newark, DE 19716

2. The Chemours Company, 201 Discovery Blvd, Newark, DE 19713

3. Department of Materials Science and Engineering, University of Delaware, Pierre S. Du Pont Hall, 127 The Green, Newark, DE 19716

4. Data Science Institute, University of Delaware, Newark DE 19716

*Corresponding author arthij@udel.edu

Table of Contents

S1. Comparison between Random Field Nafion™ Structures and Simulated Nafion™ Structures

In our recent molecular simulation work[1], we ran coarse-grained molecular dynamics (CGMD) simulations of Nafion™ membranes for a variety of ionomer designs and extents of hydration. To confirm the random field structures (which are purely based on scattering profiles and not on chemistry or polymer design) are faithful to the structures seen in CGMD simulations (which *do* account for the chemistry and polymer design), we generate random field structures from the scattering profiles computed from the molecular dynamics simulations. We then compute the size distribution, lineal path function, and tortuosity of the hydrophilic domains in the random field structures and compare these metrics to those computed from the CGMD simulations. These analyses are performed using the PoresPy package.[2] We perform this reconstruction for the polymer design $\Gamma_{sc} = 4$ (representing the number of backbone beads between each side chain), $l_{sc} = 2$ (representing the number of beads that compose each side chain), and $N_{BB} = 100$ (representing the number of beads composing the polymer's backbone). This set of parameters corresponds to an equivalent weight (EW) of 1100, and we study this system at six different levels of hydration (λ = 1, 2, 3, 6, 12, and 20) where λ=[H_2O]/[SO_3^-]. Further details about these parameters and the CGMD simulations can be found in **SI Ref. 1.**

We note that none of the CGMD simulations in our work in **SI Ref. 1.** display semi-crystallinity or globally anisotropic structures forming while the experimental measurements in the main manuscript are from Nafion™ with some crystalline domains and in some samples anisotropic structures. While this comparison of various structural features between simulation data and reconstructions reaffirms the random field model as valid for the isotropic distribution of hydrophilic domains and amorphous polymer domains, our extension to include crystalline domains has no such validation, although the approximate size and spacing of the crystalline domains is expected to be reasonable. Likewise, the anisotropy seen in our Nafion™ scattering profiles is often non-existent and, when present, is comparably minimal to other anisotropic scattering profiles, for example of polymeric materials under deformation. For this reason, in this case we believe the extension to anisotropic scattering is justifiable.

For ease of comparison between the CGMD simulations structures (which are represented as bead coordinates) and the random field reconstructions (which are represented as voxels), the CGMD simulation coordinates are converted to a voxelated representation. Each voxel is identified as one of two phases based on the identity of the nearest simulation bead: either hydrophilic (sulfonic acid group, water, hydrated counterion) or hydrophobic (polymer backbone, polymer sidechain). We compute the scattering as described in **Section S4**, radially averaging the 3D FFT to obtain the 1D scattering profile. Reconstructions are constructed based on main manuscript's **Eqs. 2-7**, with voxel sizes and total reconstruction sizes identical to the voxelated representations of the CGMD simulations. The hydrophilic volume fraction used in the reconstruction process is chosen to directly match that of the voxelated representation of the simulation.

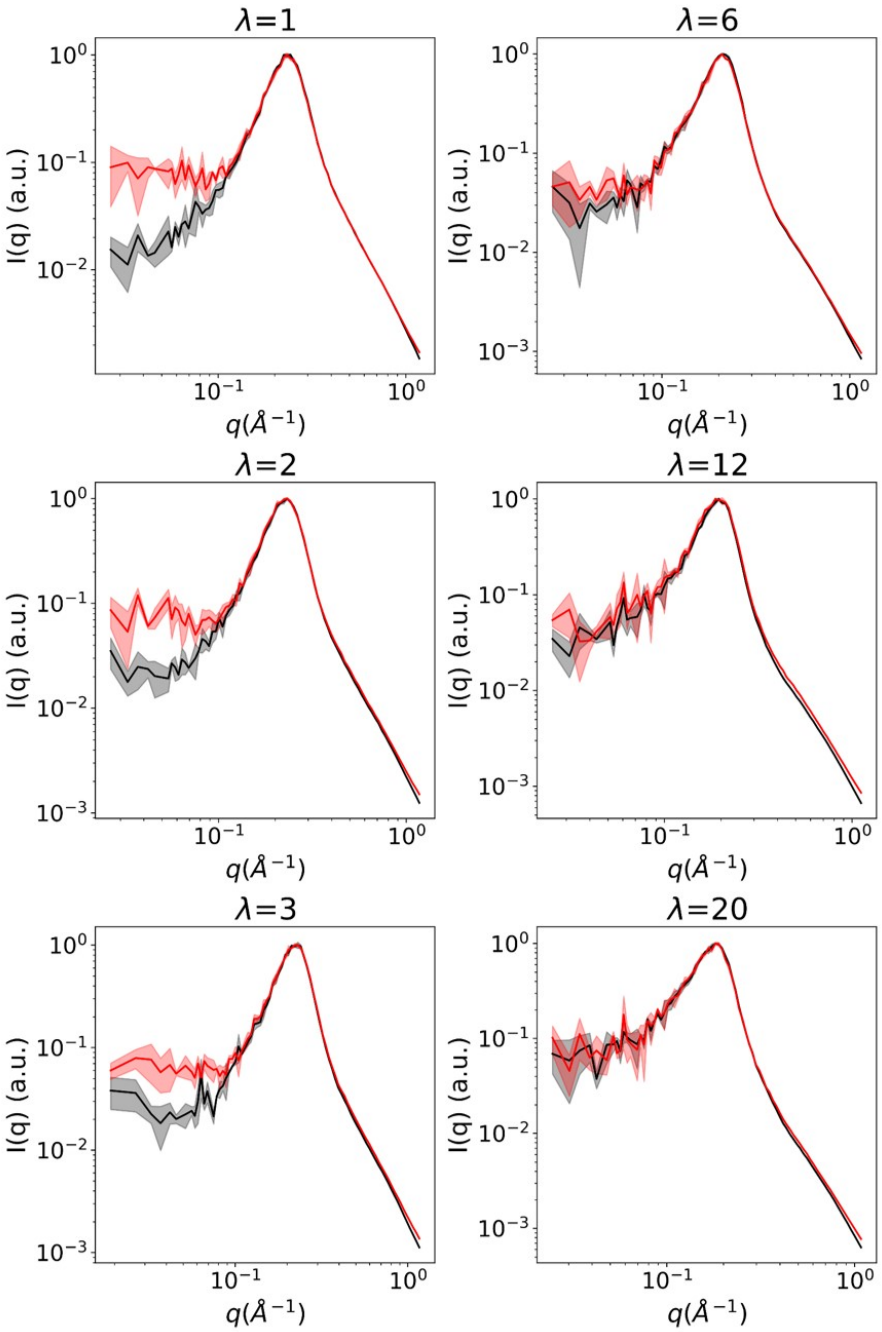

Figure S1*: Comparison of the input scattering profile computed from CGMD simulation (black) to the computed scattering profile of the reconstruction (red) at different hydrations. Shaded regions denote the standard deviation of three simulation trials/reconstructions.*

Figure S1 shows good agreement between the scattering profiles computed from the original CG MD simulations of **SI. Ref. 1** and the reconstructions from our presented approach in this main paper. We obtain a good scattering match especially at high hydration. At low hydration, the scattering intensities computed from the random field reconstructions are higher than the input

scattering from the CGMD simulations, however, the fine structure at the length scales of single clusters is still recreated well. We attribute the poor low-q fit in part to noise at low-q resulting from the finite size GGMD simulations. Visually in **Figure S2**, the reconstructions show similarity to the simulation structures.

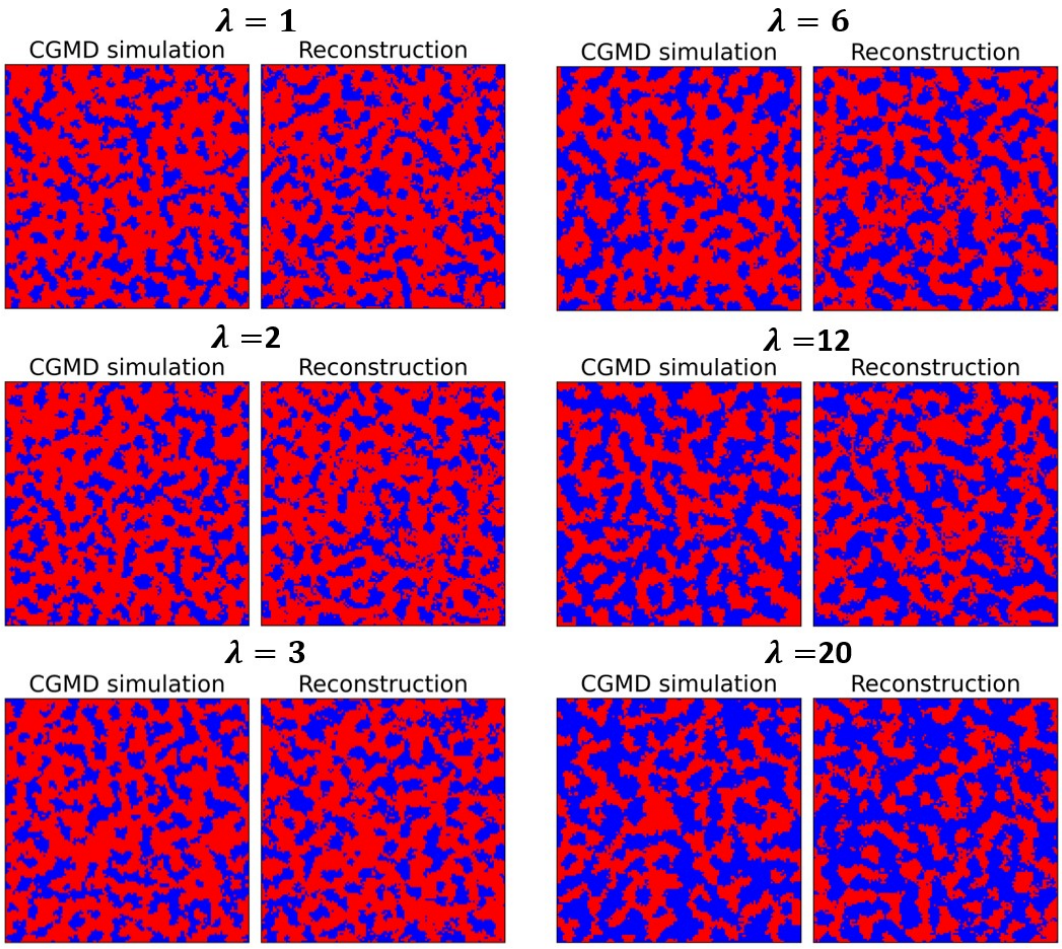

***Figure S2**: 2D slices of the voxelated CGMD simulation (left), and of the reconstruction (right) at different hydrations. Red regions denote amorphous polymer domains, and blue regions denote the hydrophilic domains. The images all represent approximately 34x34nm*

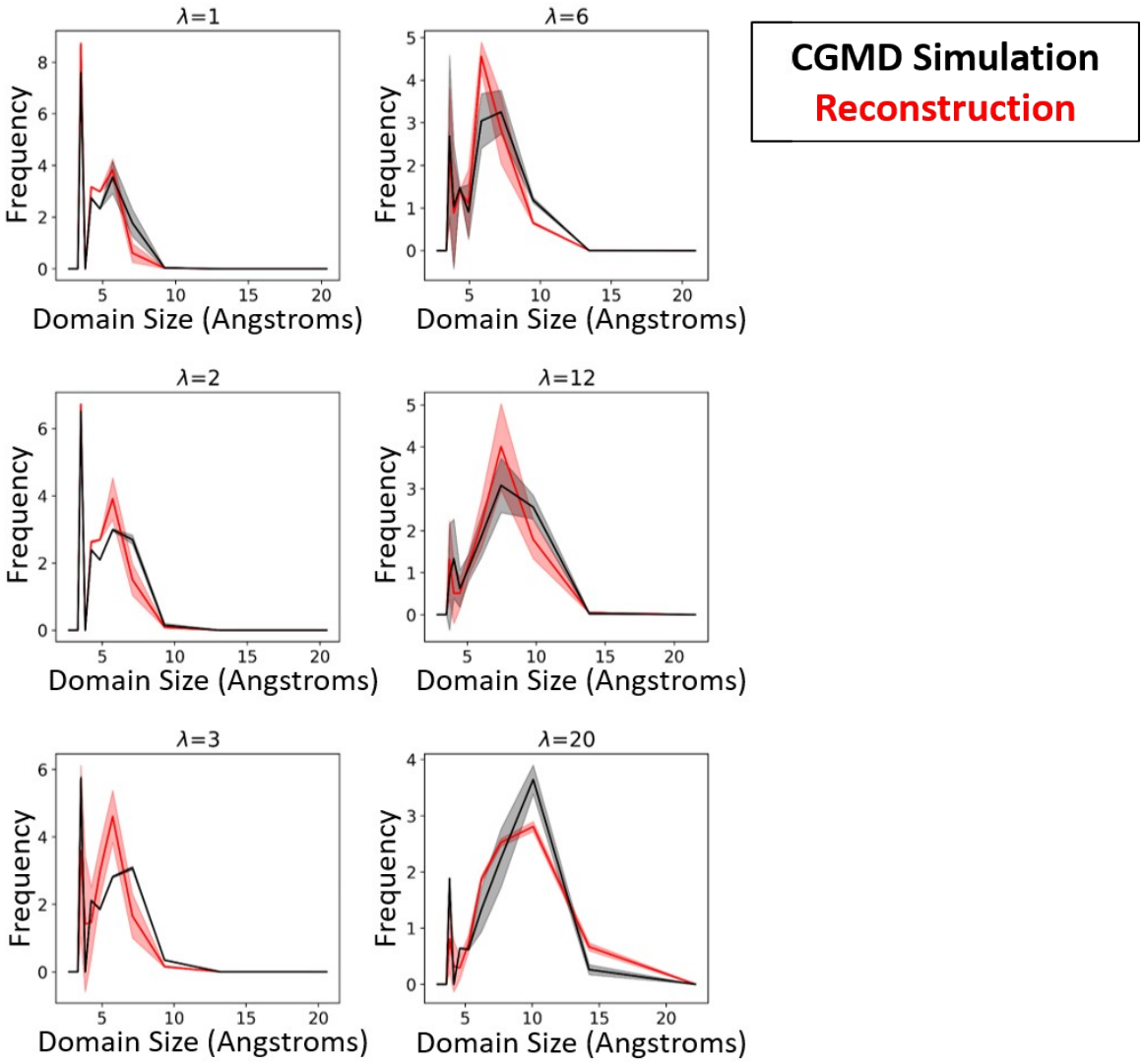

***Figure S3**: Comparisons between CGMD simulations (black curves) and reconstructions (red curves) at different levels of hydration using hydrophilic domain sizes. Shaded regions denote the standard deviation of three simulation trials/reconstructions.*

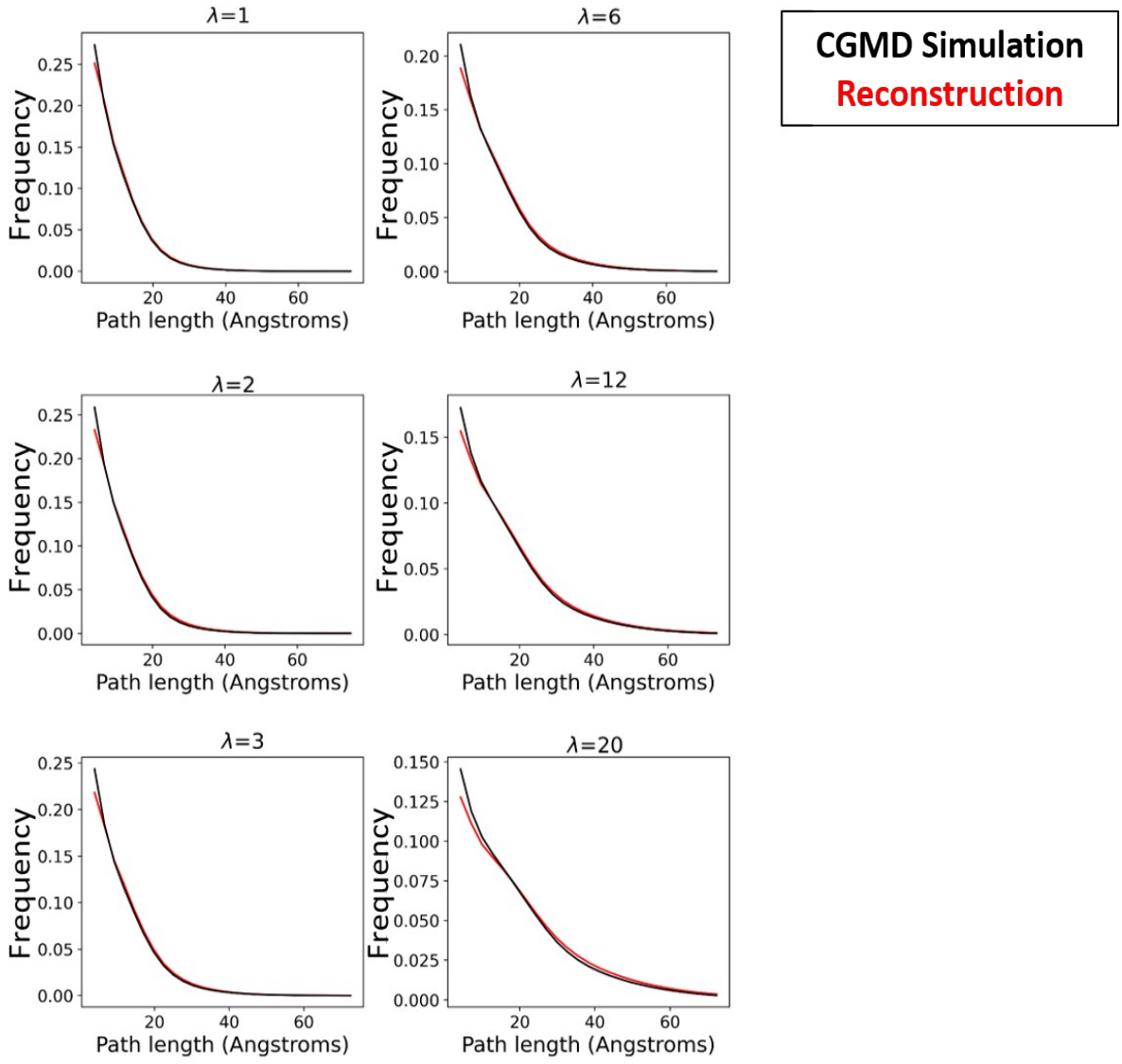

Figure S4*: Comparisons between CGMD simulations (black curves) and reconstructions (red curves) at different levels of hydration using lineal path lengths of the hydrophilic domains. Shaded regions denote the standard deviation of three simulation trials/reconstructions.*

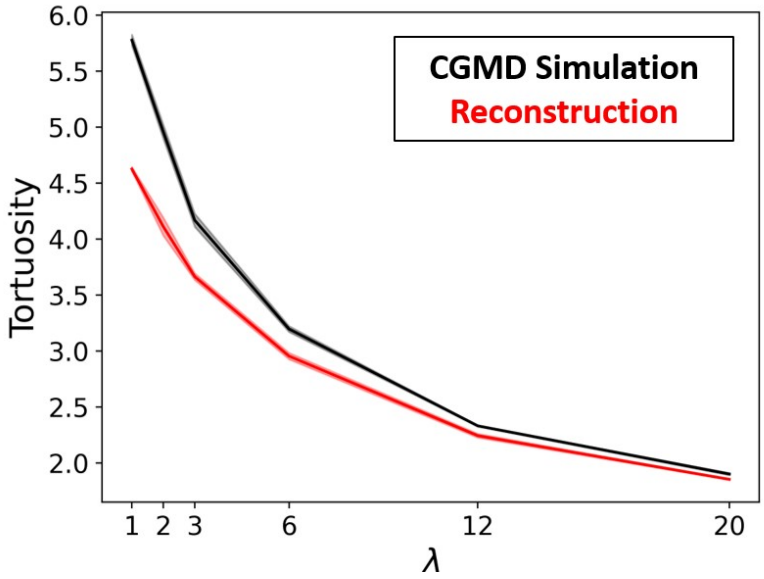

Figure S5*: Comparisons between CGMD simulations (black curves) and reconstructions (red curves) at different levels of hydration using the tortuosity of hydrophilic domains. Shaded regions denote the standard deviation of three simulation trials/reconstructions.*

In **Figure S3**, the hydrophilic domain sizes, though noisy, show qualitative agreement as λ is increased. Lineal path functions in **Figure S4** show good agreement except at small distances which is on the order of our voxel size (2.5-3Å depending on the simulation size). The tortuosity of the hydrophilic domains also qualitatively agree (**Figure S5**). The poorer match at low λ is expected as the poorer match at low-q in the scattering shown in Figure S1 indicates that we do not capture the large length-scale structure (which will directly affect the tortuosity) as well in the lower λ simulations when compared to the simulations at higher λ.

Overall, there are some discrepancies between the scattering profile and tortuosity of the reconstructions at low hydration, but the structural metrics tend to agree much better at higher hydration. As we aim to use this method to reconstruct scattering from hydrated membranes, we are not concerned with the poorer match at low hydration.

S2. Description of Numerical Implementation of the Steps in Section II of the Main Paper

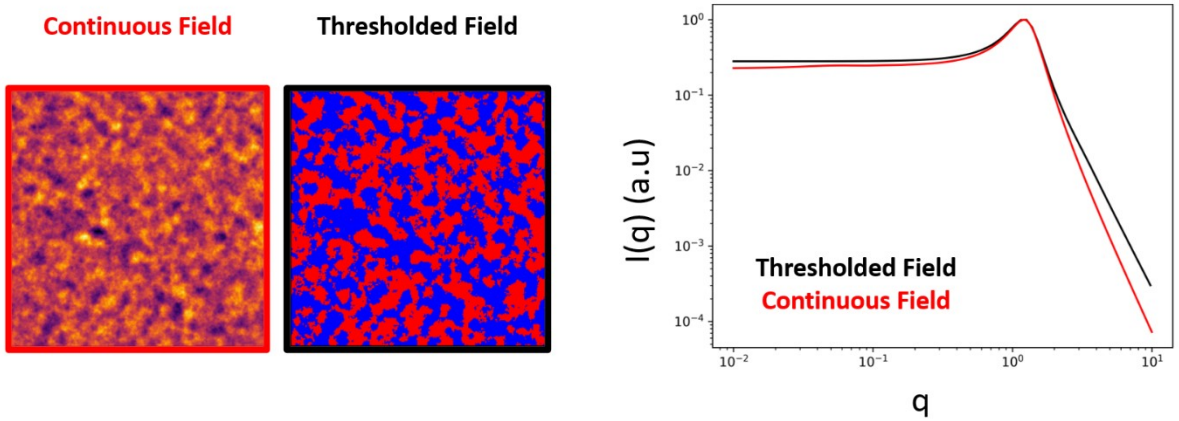

Figure S6: *Demonstration of the difference in computed scattering between a continuous random field and the same field that has been thresholded. Both scattering profiles have been normalized by the intensity of the scattering peak.*

Figure S6 demonstrates the difference in computed scattering between a continuous random field and the thresholded version of that same field (which has been thresholded at $\alpha = 0$, giving equal volume fractions of both the blue and red phases). It is readily apparent that the computed scattering is altered by the thresholding, a fact that is accounted for by Eqs. 3-7 in the main text.

A. Computation of spectral density f(q) from 1d I(q) via Main Paper's Equations 3, 4, 6, & 7

Both Eqs. 2 and 3 involve integrating from q = 0 to q = ∞, but any SAXS data only spans a finite q-range. We extrapolate the scattering curves to span the q-range spanning 10^{-7} to 10^{5}Å^{-1}. For 1D experimental scattering data, I(q), which spans the range $q_{low} \leq q \leq q_{high}$, we use the following extrapolation scheme:

$$I(q) = \begin{cases} I_{low}, & q < q_{low} \\ I(q_{high}) \left(\frac{q_{high}}{q}\right)^{m}, & q > q_{high} \end{cases}$$

Here, I_{low} is the average intensity at the five lowest data points in the original I(q). The slope of the power-law at high q, *m*, is computed by fitting the intensity of the ten highest data points in the original I(q).

$$\Gamma(r) = \frac{1}{2\pi^2} \int_0^{\infty} \left(q^2 I(q) \frac{\sin(qr)}{qr}\right) dq$$

(Main paper Eq. 3)

Simpson's method is used to evaluate the integral with 10,000 log-spaced q-points over the range 10^{-7} to 10^{5}Å^{-1}. For each value of q, $I(q)$ is evaluated by interpolating the input I(q) data using quadratic splines. This integral is evaluated for 10,000 values of r evenly spaced from 0 to 1000Å.

$$Q = \int_0^\infty q^2 I(q)\, dq$$

(Main paper Eq. 4)

Simpson's method is used to evaluate the integral at the same q-points as described for Eq. 3.

$$C_{xx}(r) = \frac{1}{2\pi} \int_0^{g(r)} \exp\left(-\frac{\alpha^2}{1+u}\right) * \frac{1}{\sqrt{1-u^2}} du$$

(Main paper Eq. 6)

The integral is evaluated for 1000 values of $g(r)$ ranging from -0.75 to 1.0 using Gaussian quadrature. Using the corresponding values of $C_{xx}(r)$ computed for each value of $g(r)$, we use quadratic spline interpolation for the function $g(r) = f(C_{xx}(r))$ to compute the value of $g(r)$ from $C_{xx}(r)$ at every value of r.

$$f(q) = \int_0^\infty (4\pi r^2 g(r) \frac{sin(qr)}{qr})\, dr$$

(Main paper Eq. 7)

Simpson's method is used to evaluate the integral with the same values of r we have used so far. This integral is evaluated for the same q-values that were used in the evaluation of Eq. 2.

Occasionally, we obtain spectral density values which are negative for certain q-values. This cannot be the case, since the methods of generating random fields (main text Eqs. 8/9) require f(q) to be non-negative. This tends to occur more frequently when the volume fraction of either phase approaches 0. We have found that generally, the negative values are small in magnitude, and setting these portions of the spectral density to 0 does not significantly change the scattering profile.

B. 3D Spectral Density Interpolation

3D interpolation is computed using the following equation, which smoothly interpolates between $f_{2D}(q_x, q_y)$ at $\varphi = \frac{\pi}{2}$ radians and $f_z(q_z)$ at $\varphi = 0$ radians:

$$f_{3D}(q_x, q_y, q_z) = f_{2D}(\rho cos\theta, \rho sin\theta)\sin^2\varphi + f_z(\rho)\cos^2\varphi$$

Here ρ, θ, and φ are the standard spherical coordinates of (q_x, q_y, q_z). f_{2D} is the two-dimensional spectral density computed from $I_{2D}(q_x, q_y)$ linearly interpolated across q_x and q_y. f_z is the assumed 1D spectral density in the z-direction, linearly interpolated across q_z.

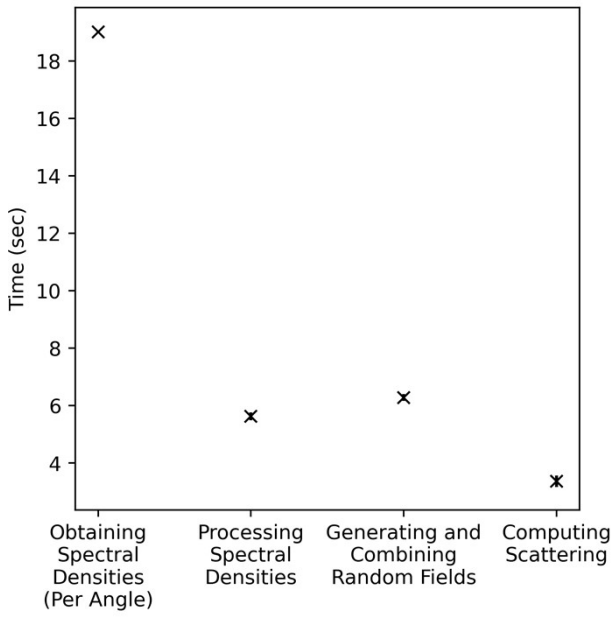

Figure S7*: Computation time for various steps of the method. Error bars indicate the standard deviation of 10 reconstruction runs.*

C. Computation Time for Different Parts of Method

In **Figure S7**, we show the computation times for the various steps of the method. Times were tracked for 10 runs of the data shown in main text **Figures 10/11** on a Dell Precision T1700 desktop computer. Because the time scale for the first step is so much larger than the following steps, we report this time normalized by the number of angles into which the original 2D scattering profile is discretized. For our case of $n_\theta = 10$, the total time for the first step is ~190 seconds. This time is primarily dependent on n_θ, as well as the number of q and r values used in the numerical integration as described above.

The time for the first two steps is an up-front cost: Once those steps have been completed (in our case ~200 seconds), as many structures as desired can be generated in ~6 seconds each. This is the time need to create 256x256x256 voxel reconstruction. If reconstructions with lower resolution are acceptable, the 6-second reconstruction time would be even less.

S3. Procedures for Obtaining and Pre-processing Small-Angle X-ray Scattering Data

A. Protocol for Obtaining SAXS data

SAXS data was obtained using the Xenocs Xeuss 2.0 SAXS/WAXS (Grenoble, France) instrument at the Advanced Material Characterization Laboratory at the University of Delaware, using a copper anode source (λ = 1.54189 Å). The sample-detector distance used was 700 mm for a collection time of 300 seconds. "Scatterless" collimation slits were set at 1.2 mm and 0.6 mm for the first and second sets, respectively. 2D images were collected using a Dectris Pilatus 3 300K detector (Baden-Daettwil, Switzerland). 2D images were not corrected for background scattering.

Dry membrane samples were conditioned at room temperature in a humidity-controlled environment (50% relative humidity) before transferred. Samples were adhered with tape to the sample holder.

Hydrated membrane samples were boiled in water for one hour and then kept enclosed in a plastic bag with excess water. Samples were sandwiched between sheets of Kapton ® with a few drops of water and compressed in the Xenocs Xeuss gel holders. The gel holders are designed to maintain solvation of gels in the vacuum environment of the x-ray instrument.

B. Preprocessing of Experimental 2-Dimensional Scattering Profiles:

The 2D scattering profiles were in the EDF file format. The EDF file contained the 2D image array that mapped the scattered intensity values on the collector plate. The header of the EDF file contained relevant information like the location of the beam center, pixel size, sample distance, etc. which were used to correctly interpret the q scale. Since the beam center is usually not at the image center, some pre-processing of the data was needed to correctly identify the data in $I(q,\theta)$ format at specific q and θ values. The first step was to recenter the image by shifting the pixel indices so that the beam center becomes the origin (0,0) in pixel coordinates. Using the knowledge that 2D scattering profiles have an inversion symmetry about the beam center $(I(q) = I(-q))$, the image can be extrapolated to obtain data for all θ values. This is achieved by considering that for a pixel index (m,n), if there is a corresponding value at $(-m,-n)$, then the two values should be averaged and used as the scattered intensity at both (m,n) and $(-m,-n)$ locations. On the other hand, if there is no value at $(-m,-n)$ due to truncation or the size of the original image, then the value at (m,n) can be copied to $(-m,-n)$. After this processing step, the pixel indices were converted to q values, by using the sample distance D, the X-ray wavelength λ and the pixel sizes (p_x,p_y). The equation to convert pixel indices (m,n) to (q_x,q_y) is written as:

$$(q_x,q_y) = \frac{4\pi}{\lambda}\left(\sin\left(\frac{1}{2}\tan^{-1}\left(\frac{mp_x}{D}\right)\right),\sin\left(\frac{1}{2}\tan^{-1}\left(\frac{np_y}{D}\right)\right)\right)$$

Subsequently, the image was cropped to a square aspect ratio such that the q ranges in the x and y directions become identical.

S4. Computation of Scattering Profiles from 3D Voxel Reconstructions

The scattering profiles of the reconstructed structures are computed using a three-dimensional fast Fourier transform (FFT) of the 3D voxel reconstruction.[3, 4]

$$I(q_x, q_y, q_z) = |F(\rho(x))|^2 P_{voxel}(q_x, q_y, q_z)^2$$

Here, F denotes the 3-dimensional fast Fourier transform, $\rho(x)$ denotes the x-ray scattering length density corresponding to the phase (hydrophilic domain, amorphous domain, or crystalline domain) at position **x**. $P_{voxel}(q_x, q_y, q_z)$ is the form factor amplitude of the cubic voxels with side length a:

$$P_{voxel}(q_x, q_y, q_z) = a^3 \frac{\sin\left(\frac{q_x a}{2}\right)\sin\left(\frac{q_y a}{2}\right)\sin\left(\frac{q_z a}{2}\right)}{\left(\frac{q_x a}{2}\right)\left(\frac{q_y a}{2}\right)\left(\frac{q_z a}{2}\right)}$$

We use the following values from that have been estimated from previous work on x-ray scattering and computational reconstructions of Nafion™ systems:[5]

$$\rho_{amorphous} = 0.548 \frac{e^-}{\text{Å}^3}$$

$$\rho_{crystalline} = 0.632 \frac{e^-}{\text{Å}^3}$$

$$\rho_{hydrophilic} = 0.334 \frac{e^-}{\text{Å}^3}$$

When computing the FFT, each voxel has a corresponding frequency defined by:

$$q_x, q_y, q_z = 2\pi\left[\frac{i - \frac{N}{2}}{Na}\right], \quad 0 \le i < N$$

where i is the index along the x, y, or z axis, N is the size of the array (number of voxels) along one dimension, and a is the voxel size in Angstroms.

The two-dimensional scattering profile is taken as the FFT intensities where the z-component of the corresponding frequency is 0 (q_z= 0). For one-dimensional scattering profiles (i.e. in **Figure S1**), the FFT intensities are radially averaged.

Because of the finite size of the reconstructions, there is generally significant noise in the computed scattering profiles at low-q. To lessen this noise, for all reported scattering calculations (except where noted), we perform 30 reconstructions and average the computed scattering profiles across all reconstructions.

S5. Resulting Structures Assuming Alternative $f(q_z) = f(q_x)$

We first show the resulting I_{rel} contours to compare them to the assumption $f(q_z) =$ azimuthal average of $f(q_x, q_y)$ in **Figure S8**. This is analogous to **Figures 8 and 9** in the main text.

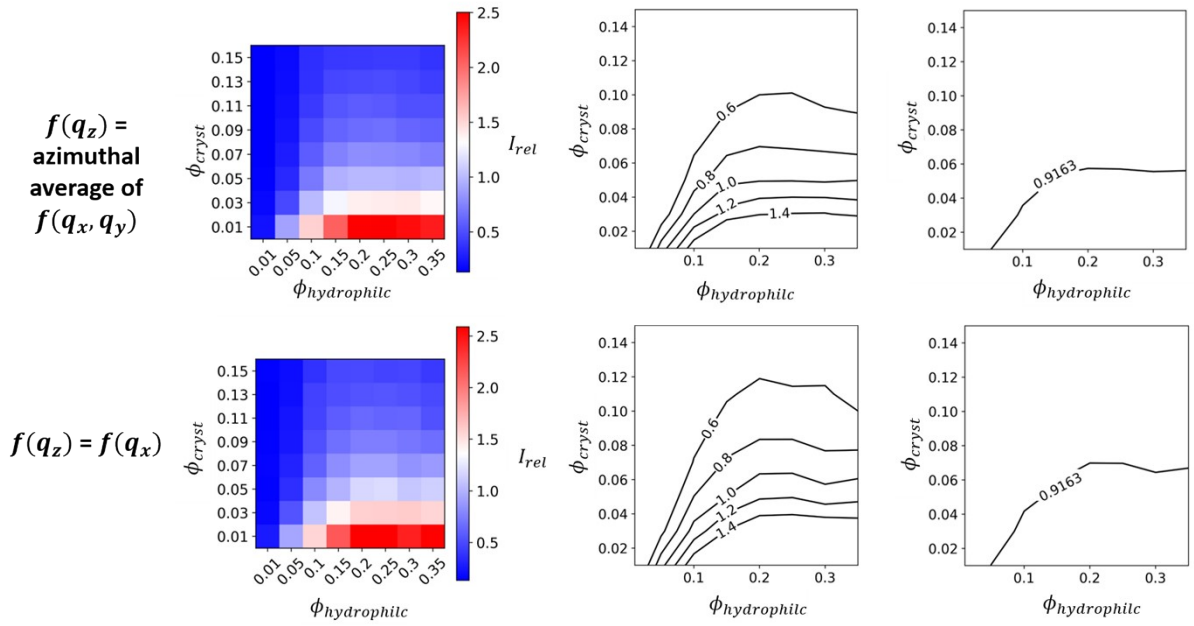

***Figure S8**: Comparison of volume fraction grid search for two different assumptions for the spectral density in the z-direction ($f(q_z)$). Top row: $f(q_z)$ = azimuthal average of $f(q_x, q_y)$. Bottom row: $f(q_z) = f(q_x)$. Left column: Heatmap showing the values of I_{rel} at varying volume fractions $\phi_{hydrophilic}$ and ϕ_{cryst}. Center column: contours at different values of I_{rel} interpolated from the grid heatmap. Right column: The interpolated contour to get a value of I_{rel} from the reconstructed scattering profile that is equivalent to the experimental h_{rel} (0.9163)*

The overall shapes of the contours are similar to those shown between the two cases. For the case where $f(q_z) = f(q_x)$, the crystalline volume fractions are higher for any given I_{rel} contour and $\phi_{hydrophilic}$, indicating that a greater fraction of the polymeric material needs to be crystalline under this assumption in comparison to the assumption that $f(q_z)$ = *azimuthal average of* $f(q_x, q_y)$. Specifically, for the experimental relative peak intensity value of 0.9163 and $\phi_{hydrophilic}$= 0.35, ϕ_{cryst} must be 0.0669 for the former case and 0.0561 for the latter case.

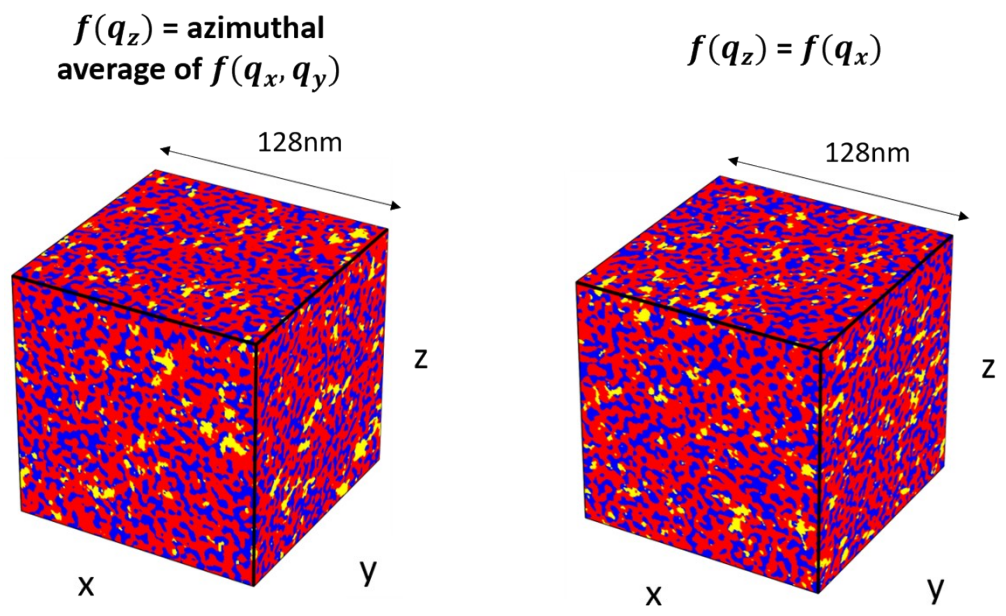

***Figure S9**: Comparison of reconstructions under two different assumptions for the spectral density in the z-direction ($f(q_z)$). Left: Reconstruction from $f(q_z)$ = azimuthal average of $f(q_x, q_y)$ (Same as main text Figure 10). Right: Reconstruction from $f(q_z) = f(q_x)$.*

We show the comparison between the reconstructions using the two different assumptions in **Figure S9**. While the differences between the two assumptions seem subtle for this case, we would expect them to become more significant if the experimental 2D scattering profile contains stronger anisotropy than what we see in our SAXS profiles of Nafion™. The structural differences are more apparent in the computed 2D scattering profiles along different axes, which are shown in **Figure S10.** While the xy-scattering are intentionally similar between the two cases (we have generated these reconstructions such that this will match the experimental scattering profile), the yz and xz-scattering show differences primarily in the matrix knee. In the yz-scattering profiles, there is a greater degree of anisotropy in the q_z direction when the $f(q_z) = f(q_x)$ assumption is made. In the xz-scattering, there is anisotropy in the z-direction for the $f(q_z)$ = azimuthal average of $f(q_x, q_y)$ assumption, but when $f(q_z) = f(q_x)$, the xz-scattering plane is isotropic, as expected.

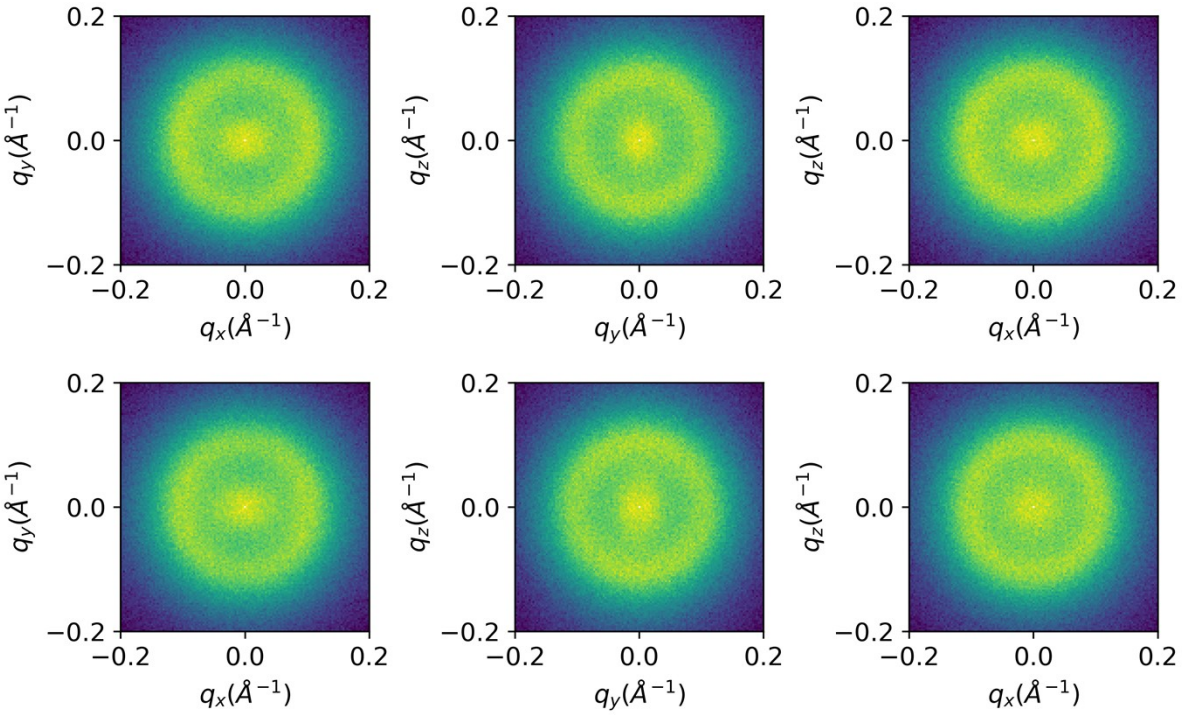

***Figure S10**: Comparison of computed scattering profiles under two different assumptions for the spectral density in the z-direction ($f(q_z)$). Top row: Reconstruction from $f(q_z)$ = azimuthal average of $f(q_x, q_y)$. Bottom row: Reconstruction from $f(q_z) = f(q_x)$. The first column corresponds to scattering perpendicular to the z-axis (which is comparable to the experimental scattering profile. The second column corresponds to scattering perpendicular to the x-axis, and the third column corresponds to scattering perpendicular to the x-axis.*

S6. Discussion/Reference Figure Regarding Field Superposition Order

The different ways to combine the two level-cut random fields are demonstrated in **Figure S11**. Because the crystalline domains are at a lower volume fraction than the hydrophilic volume fraction, the crystalline domains are more significantly affected in shape and size when the regions of intersection are assigned to the hydrophilic phase (Figure S11c). In contrast, because the hydrophilic domains are more plentiful than the crystalline domains, assigning the intersection regions to the crystalline phase minimally affects the hydrophilic domains' structure (Figure S11b). For this reason, in this work, we assign the intersection regions to the crystalline phase as in Figure S11b.

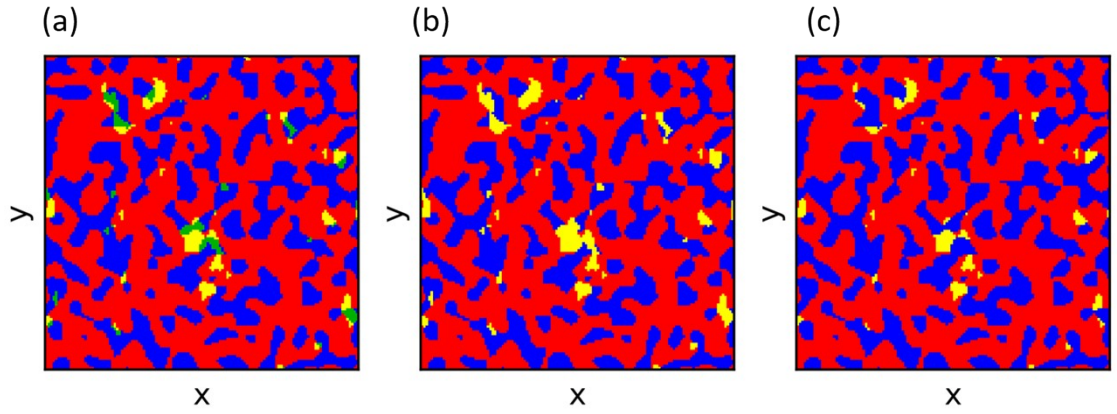

Figure S11*: 2D slices of small portions of one Nafion™ reconstruction (64x64nm window) using random fields to demonstrate how the crystalline and hydrophilic level-cut fields are combined to create the final structure. In each of a, b, and c, the red regions represent amorphous domains, the blue regions represent hydrophilic domains, and yellow regions represent crystalline domains. In a, the regions of intersection between the hydrophilic and crystalline domains are highlighted in green. In b, these regions of intersection are assigned to the crystalline phase (yellow), while in c, the regions of intersection are assigned to the hydrophilic domains (blue).*

REFERENCES

1. J. J. Madinya, S. Kronenberger, B. Gould, C. Peterson and A. Jayaraman, *Macromolecules (accepted)*.
2. J. T. Gostick, Z. A. Khan, T. G. Tranter, M. D. r. Kok, M. Agnaou, M. Sadeghi and R. Jervis, *Journal of Open Source Software*, 2019, **4**, 1296.
3. K. Schmidt-Rohr, *Journal of Applied Crystallography*, 2007, **40**, 16-25.
4. D. P. Olds and P. M. Duxbury, *Journal of Applied Crystallography*, 2014, **47**, 1077-1086.
5. S. P. Fernandez Bordín, H. E. Andrada, A. C. Carreras, G. E. Castellano, R. G. Oliveira and V. M. Galván Josa, *Polymer*, 2018, **155**, 58-63.